

# The Destabilization of Hydrogen-bonds in an External E-Field for Improved Switch Performance

Tianlv Xu<sup>1</sup>, Roya Momen<sup>1</sup>, Alireza Azizi<sup>1</sup>, Tanja van Mourik<sup>2</sup>, Herbert Früchtl<sup>2</sup>, Steven R. Kirk<sup>\*1</sup> and Samantha Jenkins<sup>\*1</sup>

<sup>1</sup>*Key Laboratory of Chemical Biology and Traditional Chinese Medicine Research and Key Laboratory of Resource National and Local Joint Engineering Laboratory for New Petro-chemical Materials and Fine Utilization of Resources, College of Chemistry and Chemical Engineering, Hunan Normal University, Changsha, Hunan 410081, China*

<sup>2</sup>*EaStCHEM School of Chemistry, University of St Andrews, North Haugh, St Andrews, Fife KY16 9ST, Scotland, United Kingdom.*

\*email: samanthajsuman@gmail.com

\*email: steven.kirk@cantab.net

The effect of an electric field on a recently proposed molecular switch based on a quinone analogue was investigated using next-generation quantum theory of atoms in molecules (QTAIM) methodology. The reversal of a homogenous external electric field was demonstrated to improve the ‘OFF’ functioning of the switch. This was achieved by destabilization of the H atom participating in the tautomerization process along the hydrogen bond that defines the switch. The ‘ON’ functioning of the switch, from the position of the tautomerization barrier, is also improved by the reversal of the homogenous external electric field: this result was previously inaccessible. The ‘ON’ and ‘OFF’ functioning of the switch was visualized in terms of the response of the most preferred directions of motion of the electronic charge density to the applied external field. All measures from QTAIM and the stress tensor provide consistent results for the factors affecting the ‘ON’ and ‘OFF’ switch performance. Our analysis therefore demonstrates use for future design of molecular electronic devices.

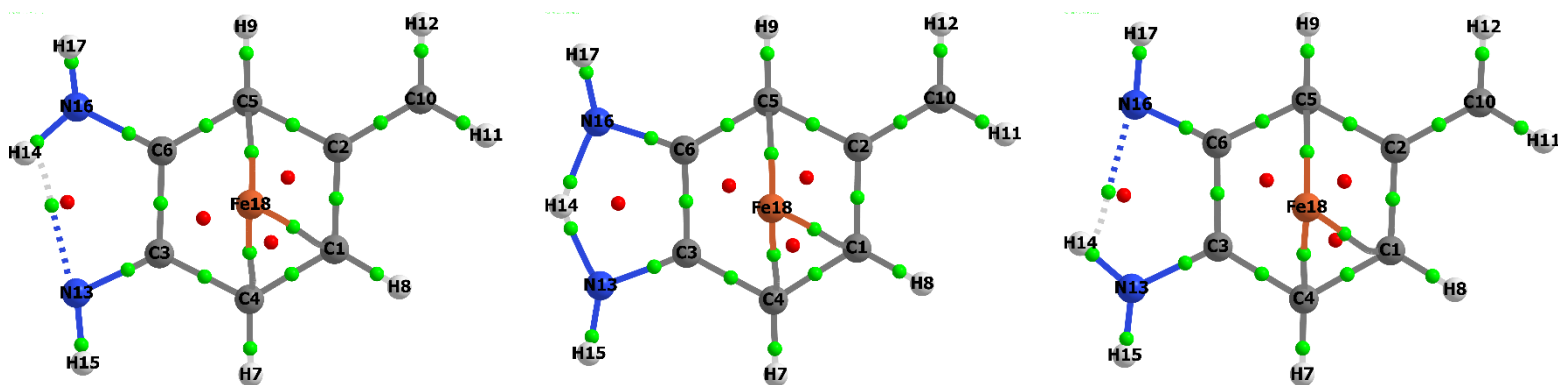
## 1. Introduction

The first theoretical and experimental efforts in molecular electronics were introduced by Aviram and Ratner in the 1970s<sup>[1]</sup>. Constructing an electronic device using individual atoms and/or molecules remains one of the ultimate goals in electronics<sup>[2]</sup>. With miniaturization of semiconductor devices as described by Moore's Law<sup>[3]</sup> reaching its physical limits, the single-molecule-junction research field is currently attracting increased interest, and various techniques are being developed to connect small ensembles of molecules<sup>[4]</sup>. Various molecules have been investigated for their potential use as molecular switches<sup>[5]</sup>. The interaction of molecules with external fields, static or time dependent, can significantly alter the potential energy surfaces (PES) governing chemical reactions, that is, the breaking and making of chemical bonds<sup>[6]</sup>. In 2003, researchers developed a statistical approach to determine the conductance of a single-molecule junction using a scanning tunneling microscope (STM)<sup>[7]</sup>.

One recently proposed class of molecular switches consists of quinone derivatives with and without a coordinated metal atom<sup>[8]</sup> and with adjacent imino and amino groups, where the switching mechanism is based on the exchange of a hydrogen atom between these groups, corresponding to the 'ON' and 'OFF' position of the switch. Other switchable single molecular devices have been proposed, for instance comprising the ellipsoidal fullerene C<sub>70</sub><sup>[9]</sup>

We investigated the functioning of such a quinone switch and found that the addition of the Fe-dopant led to a more symmetrical relative energy barrier for the hydrogen transfer<sup>[10]</sup>. Consequently, it was found that the undoped quinone switch was 'leakier' compared with the Fe-doped switch due to the higher position of the forward minimum relative to the reverse minimum. This meant that the undoped switch was less able to fully attain the 'OFF' position than the Fe-doped switch.

For the current work we chose a further simplified molecule with only one amino-imino connection, as shown in **Scheme 1**. We consider the effect of applying an electric field that is varied in magnitude and direction on the functioning of the switch, i.e. the transfer of the hydrogen marked H14 in **Scheme 1**.



**Scheme 1.** The molecular graphs corresponding to the reverse minimum, the transition state and the forward minimum are presented moving from left to right. The undecorated green and red spheres represent the bond critical points (BCPs) and ring critical points (RCPs) respectively. The positive and negative directions of the external **E**-field correspond to the C1-C2 and C2-C1 bond-path directions respectively.

The effect on the chemical bond of external homogenous **E**-fields can significantly alter the potential energy surfaces (PES) controlling chemical reactions involved with the formation and rupture of chemical bonds<sup>[11–15]</sup>. Previously, Sowlati-Hashjin and Matta undertook an investigation of strong external homogenous **E**-fields ( $\pm 10 \times 10^9 \text{ Vm}^{-1}$ ). They found that parallel **E**-fields increasingly stretch a bond with increasing **E**-field strength; conversely antiparallel fields compress the bond but to a lesser extent<sup>[16]</sup>. In this investigation we will use smaller external **E**-fields in the range  $\pm 40 \times 10^4 \text{ au} \approx \pm 2.1 \times 10^9 \text{ Vm}^{-1}$  that would be more easily accessible experimentally, for example within an STM. Other work of note on the effect of external **E**-fields on chemical bonds is provided by Saenz<sup>[17–19]</sup> and more recent investigations by Foroutan-Nejad *et al.* including charged systems<sup>[20–22]</sup>.

The main goal of this study is to understand both the ‘ON’ and the ‘OFF’ switching performance as a function of an oriented external **E**-field, on the model system shown in **Scheme 1**. Examination of the energy barrier only enables an understanding of (either) the ‘OFF’ switch performance or the ‘ON’ position, as a function of the applied **E**-field, see the forward and reverse minimum respectively in **Figure 1**. For instance, in the ‘ON’ position the applied **E**-field cannot be used to distinguish the effects on the PES of varying the **E**-field on the PES. It is worth noting that oriented **E**-fields have recently been suggested to perform as smart catalysts by Shaik *et al*<sup>[23–25]</sup>.

Next generation QTAIM and the stress tensor methodology that includes a 3-D, non-minimal three-stranded directional interpretation of bonding incorporates the *most* preferred direction of electronic charge density accumulation. This directional approach can be used in a variety of circumstances where conventional QTAIM, that only provides scalar measures such as bond ellipticity  $\varepsilon$ , is not useful. Examples that highlight the utility of this directional approach of next generation QTAIM include understanding the consequences of application of external forces, e.g. normal modes<sup>[26]</sup> excited states and torsions<sup>[27–29]</sup>.

In section 2 we summarize the necessary background theory, with the more detailed derivations and discussions being provided in the **Supplementary Materials S1**. The basic computational details are given in section 3, with more complex procedure being provided in the **Supplementary Materials S2**. The results and discussion are presented in section 4 and finally the conclusions are presented in section 5.

## 2. Theory and Methods

### 2.1 The QTAIM and stress tensor BCP descriptors; ellipticity $\varepsilon$ , the total local energy density $H(\mathbf{r}_b)$ and stress tensor eigenvalue $\lambda_{3\sigma}$ and stress tensor trajectories $\mathbb{T}_\sigma(s)$

We use QTAIM<sup>[30]</sup> and the stress tensor analysis that utilizes higher derivatives of the total charge density distribution  $\rho(\mathbf{r}_b)$  at the bond critical point (BCP) where the subscript ‘**b**’ refers to the BCP., in effect acting as a ‘magnifying lens’ on the  $\rho(\mathbf{r}_b)$  derived properties of the wave-function. QTAIM allows us to identify critical points in the total electronic charge density distribution  $\rho(\mathbf{r})$  by analyzing the gradient vector field  $\nabla\rho(\mathbf{r})$ . These critical points can be divided into four types of topologically stable critical points according to the set of ordered eigenvalues  $\lambda_1 < \lambda_2 < \lambda_3$ , with corresponding eigenvectors  $\mathbf{e}_1$ ,  $\mathbf{e}_2$ ,  $\mathbf{e}_3$  of the Hessian matrix.

In the limit that the forces on the nuclei become vanishingly small, an atomic interaction line (AIL)<sup>[31]</sup> becomes a bond-path, although not necessarily a chemical bond<sup>[32]</sup>. The complete set of critical points together with the bond-paths of a molecule or cluster is referred to as the molecular graph, with the constituent atoms being referred to as nuclear critical points (NCPs). The ellipticity  $\varepsilon$  provides the relative accumulation of  $\rho(\mathbf{r}_b)$  in the two directions perpendicular to the bond-path at a BCP, defined as  $\varepsilon = |\lambda_1|/|\lambda_2| - 1$  where  $\lambda_1$  and  $\lambda_2$  are negative eigenvalues of the corresponding  $\mathbf{e}_1$  and  $\mathbf{e}_2$  respectively. It has been shown<sup>[33,34]</sup> that the degree of covalent character can be determined from the total local energy density  $H(\mathbf{r}_b)$ , defined as:

$$H(\mathbf{r}_b) = G(\mathbf{r}_b) + V(\mathbf{r}_b) \quad (1)$$

In equation (1),  $G(\mathbf{r}_b)$  and  $V(\mathbf{r}_b)$  are the local kinetic and potential energy densities at a BCP, respectively. A value of  $H(\mathbf{r}_b) < 0$  for the closed-shell interaction,  $\nabla^2\rho(\mathbf{r}_b) > 0$ , indicates a BCP with a degree of covalent character, and conversely  $H(\mathbf{r}_b) > 0$  reveals a lack of covalent character for the closed-shell BCP. In the terminology used throughout this work, ‘--’ refers to closed-shell BCPs which by definition always possess values of the Laplacian  $\nabla^2\rho(\mathbf{r}_b) > 0$ , but can possess  $H(\mathbf{r}_b) < 0$  or  $H(\mathbf{r}_b) > 0$ . An example includes the H14--N13 BCP, see the left panel of **Scheme 1**. Conversely ‘-’ always refers to shared-shell BCPs which by definition always possess values of the Laplacian  $\nabla^2\rho(\mathbf{r}_b) < 0$  and  $H(\mathbf{r}_b) < 0$ , e.g. the N13-H14 BCP, see the right panel of **Scheme 1**. A related quantity to the ellipticity  $\varepsilon$  for closed-shell interactions is the metallicity:

$$\xi(\mathbf{r}_b) = \rho(\mathbf{r}_b)/\nabla^2\rho(\mathbf{r}_b) \geq 1, \quad (2)$$

In equation (2) the values of total electronic charge density  $\rho(\mathbf{r}_b)$  and the Laplacian  $\nabla^2\rho(\mathbf{r}_b)$  are calculated at the BCP. The metallicity  $\xi(\mathbf{r}_b)$ <sup>[35,36]</sup>, previously has been used to explore suspected metallicity ranges of metals, metalloids and non-metals<sup>[35,36]</sup>. Some of the current authors also demonstrated that the  $\xi(\mathbf{r}_b)$  is inversely related to “nearsightedness” of the first-order density matrix and is suitable for closed-shell systems<sup>[37]</sup>. In this investigation we will use the metallicity  $\xi(\mathbf{r}_b)$  to explain the functioning of the switch in terms of the changes to the  $\xi(\mathbf{r}_b)$  values as a function of the oriented external  $\mathbf{E}$ -field during the tautomerization process of the H atom along the hydrogen bond.

The quantum stress tensor,  $\sigma(\mathbf{r})$ , is directly related to the Ehrenfest force by the virial theorem and so provides a physical explanation of the low frequency normal modes that accompany structural rearrangement<sup>[38-40]</sup>. In this investigation we will use Bader’s definition<sup>[41,42]</sup> of the stress tensor. A diagonalization of the stress tensor,  $\sigma(\mathbf{r})$ , returns the principal electronic stresses. The stress tensor eigenvalue associated with the bond path,  $\lambda_{3\sigma}$ , has been associated with transition-type behavior in molecular motors<sup>[43]</sup>. The stress tensor eigenvectors  $\mathbf{e}_{1\sigma}$  and  $\mathbf{e}_{2\sigma}$  correspond to the most and least preferred directions of

charge density accumulation  $\rho(\mathbf{r}_b)$ , and the  $\mathbf{e}_{3\sigma}$  eigenvector is always directed along the bond path. The stress tensor eigenvector trajectories  $\mathbb{T}_\sigma(s)$  are constructed from the set of shifts  $\mathbf{dr}(s)$ , associated with steps  $s$ , where the parameter  $s$  is a sequence number of a given *BCP* in 3-D Cartesian space as an ordered set of vectors  $\mathbf{dr}'(s)$  in the stress tensor eigenvector projection space  $\mathbb{U}_\sigma$ . Earlier, for a series of competitive ring-opening reactions, some of the current authors found a *BCP* that moves further relative to the  $\{\mathbf{e}_{1\sigma}, \mathbf{e}_{2\sigma}, \mathbf{e}_{3\sigma}\}$  framework at the transition state of that *BCP*, i.e. with a longer  $l$  signifying the attainment of a lower transition state energy barrier than a *BCP* trajectory  $\mathbb{T}_\sigma(s)$  with a shorter  $l^{[44]}$ . The real-space lengths  $l(s)$  of the  $\mathbb{T}_\sigma(s)$  are calculated as the sum:

$$l = \sum_s |\mathbf{dr}(s)| \quad (3)$$

The procedure used to generate the  $l$  is provided in the **Supplementary Materials S2**.

We also previously used the stress tensor eigenvectors  $\{\mathbf{e}_{1\sigma}, \mathbf{e}_{2\sigma}, \mathbf{e}_{3\sigma}\}$ , instead of the Cartesian coordinate frame, to track and characterize the changing orientation of the eigenvectors of the *BCPs* with respect to the functioning of the quinone switch<sup>[10]</sup> in the presence or absence of an Fe-dopant atom. These were compared with the symmetry of the relative energy barrier, with the Fe-dopant increasing the symmetry relative to the undoped switch. We visualized the stress tensor  $\mathbb{T}_\sigma(s)$  trajectories starting from the transition state (switch neither ‘ON’ nor ‘OFF’) and ending at the minimum corresponding to the reverse = ‘ON’ or forward = ‘OFF’ switch positions.

In this investigation we do not consider varying the presence of dopants or atomic substituents on the functioning of the switch; instead we examine the effect of varying an external electric field  $\mathbf{E} = 0, \pm 20 \times 10^{-4}$  au and  $\pm 40 \times 10^{-4}$  au. We will use the real-space length  $l$  of the *BCP* trajectory  $\mathbb{T}_\sigma(s)$  to examine the switch functioning, i.e. the ‘ON’ and ‘OFF’ switch positions, for direct comparison with the calculated relative energy  $\Delta E$  along of the IRC (internal reaction coordinate). In addition, since the H14 *NCP* is confined to move along the N16 *NCP* and N13 *NCP*, we will introduce for the first time, the *NCP* trajectory  $\mathbb{T}_\sigma(s)$  and use it to examine directly the motion of the facile H14 *NCP*.

## 2.2 The QTAIM bond-path properties; the bond-path framework set $\mathbb{B}$

The bond-path length (BPL) is defined as the length of the path traced out by the  $\mathbf{e}_3$  eigenvector of the Hessian of the total charge density  $\rho(\mathbf{r})$ , passing through the *BCP*, along which  $\rho(\mathbf{r})$  is locally maximal with respect to any neighboring paths. The bond-path curvature is a dimensionless ratio separating two bonded nuclei and is defined as:

$$(\text{BPL} - \text{GBL})/\text{GBL} \quad (4)$$

In Equation (4) the geometric bond length (GBL) refers to the inter-nuclear separation. The BPL can exceed the GBL for weak or strained bonds existing in unusual bonding environments<sup>[45]</sup>. For 3-D bond-paths, there are minor and major radii of bonding curvature, specified by the directions of  $\underline{e}_2$  and  $\underline{e}_1$  respectively<sup>[46]</sup>.

We refer to the next-generation QTAIM interpretation of the chemical bond as the *bond-path framework set*, denoted by  $\mathbb{B}$ , where  $\mathbb{B} = \{p, q, r\}$ , with the consequence that for a given electronic state a bond is comprised of three ‘linkages’;  $p$ ,  $q$  and  $r$  associated with the  $\underline{e}_1$ ,  $\underline{e}_2$  and  $\underline{e}_3$  eigenvectors, respectively. Here the  $p$  and  $q$  are 3-D paths constructed from the values of the least ( $\underline{e}_1$ ) and most ( $\underline{e}_2$ ) preferred directions of electronic charge density accumulation  $\rho(\mathbf{r})$  along the bond-path, referred to as ( $r$ ). An in depth discussion with derivations of  $\mathbb{B} = \{p, q, r\}$  is provided in the **Supplementary Materials S1**.

The orbital-like *packet* shapes that the pair of  $q$ - and  $q'$ -paths form along the *BCP* are referred to as a  $\{q, q'\}$  path-packet. Extremely long  $\{q, q'\}$ -paths indicate the imminent rupture caused by the coalescence of a *BCP* with the associated *RCP*. Larger  $\{q, q'\}$  and  $\{q_{\sigma}, q'_{\sigma}\}$  path-packets in the vicinity of a *BCP* signify an easier passage of the *BCP* and hence of the associated H14 *NCP* as opposed to smaller  $\{q, q'\}$  and  $\{q_{\sigma}, q'_{\sigma}\}$ -path packets.

The  $\{p, p'\}$  and mixed  $\{p, q\}$  path-packets are provided in **Supplementary Materials S3**. The path-packets corresponding to the Fe-dopant are provided in **Supplementary Materials S4**. The stress tensor  $\{p_{\sigma}, p'_{\sigma}\}$  and the mixed  $\{p_{\sigma}, q_{\sigma}\}$  path-packets are provided in **Supplementary Materials S5**.

### 3. Computational Details

Candidate structures for transition states were optimized with Gaussian 09<sup>[47]</sup> using DFT at the PBE<sup>[48]</sup>/cc-pVTZ<sup>[49]</sup> level of theory, with Grimme's empirical 3-center dispersion correction with Becke-Johnson damping<sup>[50,51]</sup>. Gaussian's 'ultrafine' DFT integration grid was used for all calculations. These settings were retained in all subsequent calculations described below. The presence of exactly one imaginary vibrational frequency was confirmed for each transition state structure. All IRC calculations were performed with a step size of 0.03 Bohr, tight SCF convergence criteria and a termination criterion of energy gradient magnitude  $< 2 \times 10^{-4}$  Hartree/Bohr. The final calculated structures on each IRC path were then used as starting points for standard geometry optimizations, using the same method, basis set and DFT settings, to obtain precise local energy minimum structures to complete each full IRC path. For each generated structure representing a point on each computed IRC path, single-point SCF calculations were performed with the aforementioned DFT settings and basis set, with additional stricter convergence criteria;  $< 10^{-10}$  RMS change in the density matrix and  $< 10^{-8}$  maximum change in the density matrix. These calculations yielded the wave-functions needed for QTAIM analysis. Calculations of the molecular graphs and critical point properties were performed using AIMAll<sup>[52]</sup> all molecular graphs were additionally confirmed to be free of non-nuclear attractor critical points.

## 4. Results and Discussion

### 4.1 The switching performance from QTAIM and stress tensor BCP measures

Examination of the relative energy  $\Delta E$  demonstrates the effect of both the magnitude and direction of the external  $\mathbf{E}$ -field on the shape of the barrier, see **Figure 1**. The reverse (negative IRC coordinate) and forward (positive IRC coordinate) directions correspond to the ‘ON’ and ‘OFF’ positions of the switch respectively. The effect of an increase in the magnitude of the  $\mathbf{E}$ -field in the positive direction (parallel to the C1-C2 BCP bond-path ( $\mathbf{r}$ )) is to create a more symmetrical relative energy barrier, relative to the absence of the external  $\mathbf{E}$ -field, leading to more favorable switch behavior, see **Scheme 1**. Conversely, an increase in the magnitude of the  $\mathbf{E}$ -field in the negative direction (anti-parallel to the C1-C2 BCP bond-path ( $\mathbf{r}$ )) renders the barrier less symmetrical therefore causing less favorable switch behavior.

The hydrogen bonds corresponding to the H14--N13 BCP and H14--N16 BCP are present for the reverse (switch ‘ON’ position) and forward (switch ‘OFF’ position) minima respectively, see **Scheme 1**.

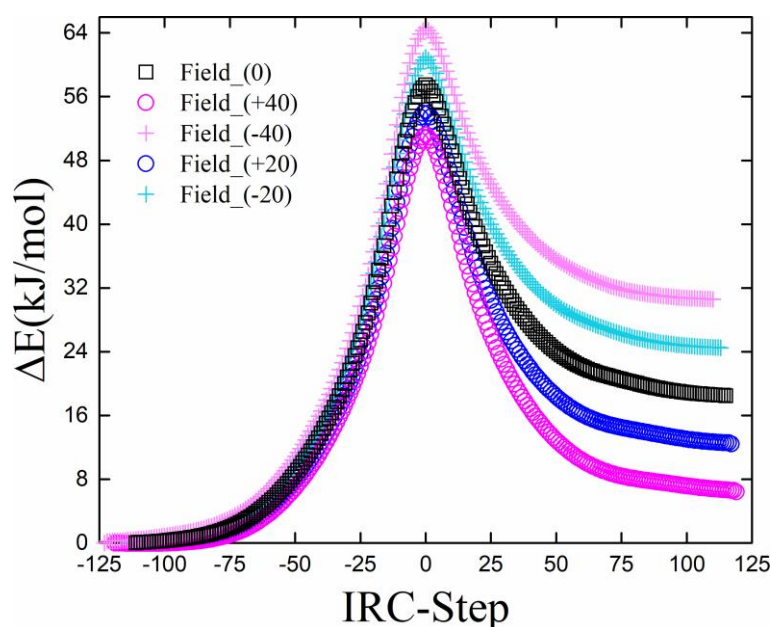


**Figure 1.** The variation of the relative energy  $\Delta E$  along the IRC with the oriented external electric field  $\mathbf{E} = -40 \times 10^{-4}$  au (64.51 kJ/mol),  $-20 \times 10^{-4}$  au (60.91 kJ/mol), 0 au (57.45 kJ/mol),  $+20 \times 10^{-4}$  au (54.22 kJ/mol) and  $+40 \times 10^{-4}$  au (51.20 kJ/mol), where the barrier heights are indicted in brackets. The reverse minimum and forward minimum correspond to the switch ‘ON’ and ‘OFF’ positions respectively, see **Scheme 1**.

From QTAIM, examination of the total local energy density  $H(\mathbf{r}_b)$  plots indicate that larger positive  $\mathbf{E}$ -field values decrease the strength of the H14--N13/N13-H14 BCP and N16-H14/H14--N16 BCP (more negative values of  $H(\mathbf{r}_b)$ ), see **Figure S6(a)** and **Figure S6(b)** of the **Supplementary Materials S6**. Consistency is found from the stress tensor eigenvalue  $\lambda_{3\sigma}$ , with more positive values of  $\lambda_{3\sigma}$  (i.e. greater topological stability) correlating with more negative values of  $H(\mathbf{r}_b)$ , see the **Supplementary Materials S7**. The  $H(\mathbf{r}_b)$  and  $\lambda_{3\sigma}$  results demonstrate that the H14--N16 BCP weakens and is destabilized by an increase in the (+) $\mathbf{E}$ -field. The converse is true for an increase in the applied (-) $\mathbf{E}$ -field, i.e. the H14--N16 BCP is strengthened

and stabilized. Similarly, the  $H(\mathbf{r}_b)$  and  $\lambda_{3\sigma}$  values show that this time the H14--N13/N13-H14 *BCP* is weakened and destabilized by an increase in the (-) $\mathbf{E}$ -field. Therefore, the ‘OFF’ switch performance that corresponds to the H14--N16 *BCP* is increased/reduced by the increase in the magnitude of the (+) $\mathbf{E}$ -field/(-) $\mathbf{E}$ -field. Conversely, the ‘ON’ switch performance that corresponds to the H14--N13 *BCP* is increased/reduced by the increase in the magnitude of the (-) $\mathbf{E}$ -field/(+) $\mathbf{E}$ -field.

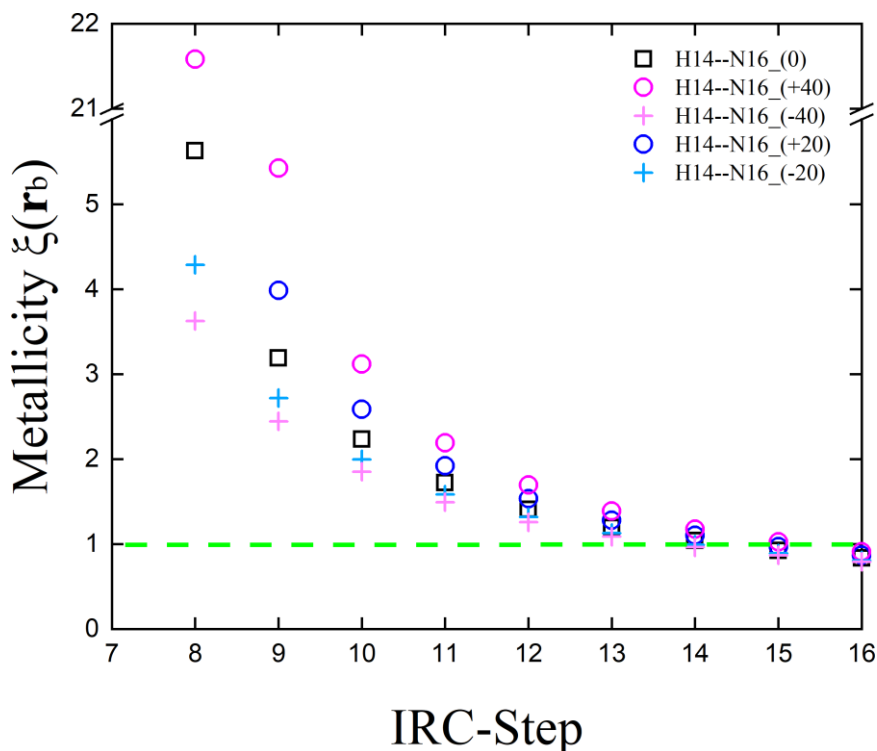


**Figure 2.** The variation of the metallicity  $\xi(\mathbf{r}_b)$  with the IRC from the transition state at IRC-Step = 0 towards the forward minimum for the H14--N16 *BCP* for values of the external electric field  $\mathbf{E} = 0, \pm 20 \times 10^{-4}$  au and  $\pm 40 \times 10^{-4}$  au, see **Scheme 1**. The horizontal green dash-line indicates values of metallicity  $\xi(\mathbf{r}_b) = 1.0$ .

The metallicity  $\xi(\mathbf{r}_b)$  will now be used to investigate the destabilization/stabilization of the H16--N14 *BCP* due to the external  $\pm \mathbf{E}$ -field. The progress of the H14 *NCP* away from the transition state during the tautomerization process leads to the creation of the metallic H16--N14 *BCP*, indicated by the presence of values of the metallicity  $\xi(\mathbf{r}_b) \geq 1$ , see **Figure 2**. The application of the non-zero  $\mathbf{E}$ -fields;  $\mathbf{E} = \pm 20 \times 10^{-4}$  and  $\mathbf{E} = \pm 40 \times 10^{-4}$  au, leads to significant variation in the metallicity  $\xi(\mathbf{r}_b)$  values of the H16--N14 *BCP*. Larger (+) $\mathbf{E}$ -fields correlate with higher  $\xi(\mathbf{r}_b)$  values further away from the transition; the converse is true for more negative (-) $\mathbf{E}$ -fields consistent with the stabilities determined by the relative energy  $\Delta E$  for the forward direction, see **Figure 1**.

**Table 1.** The variation of the  $\Delta(BCP-RCP)$  in au corresponding to the reverse (r) minimum, transition state and forward (f) minimum for values of the  $\mathbf{E}$ -field =  $\pm 20 \times 10^{-4}$  au and  $\pm 40 \times 10^{-4}$  au where the  $\mathbf{E} = 0$  values are subtracted in each case, see **Scheme 1**. The separation  $BCP-RCP = 0.096$  au for the Fe18--C3  $BCP$ , only exists for the f minimum, corresponds to an external  $\mathbf{E}$ -field of value  $-40 \times 10^{-4}$  au. We use the bond notation “-“ and “--“ to denote a shared-shell  $BCP$  and a closed-shell  $BCP$  respectively.

$BCP$	$\Delta(BCP-RCP)$	
	-20	+20
H14--N13/N13-H14	{(-0.100, 0.006, -0.006)}	{( 0.077, -0.006, 0.006)}
N16-H14/H14--N16	{( 0.002, -0.006, 0.051)}	{(-0.004, 0.006, -0.060)}
Fe18--C1	{( 0.009, -0.004, -0.040)}	{(-0.009, 0.002, 0.028)}
Fe18--C4	{(-0.009, 0.002, 0.025)}	{( 0.009, 0.002, -0.021)}
	-40	+40
H14--N13/N13-H14	{(-0.300, 0.009, -0.011)}	{( 0.142, -0.009, 0.011)}
N16-H14/H14--N16	{(-0.011, -0.011, 0.096)}	{(-0.009, 0.009, -0.136)}
Fe18--C1	{( 0.017, -0.011, -0.098)}	{(-0.019, 0.000, 0.051)}
Fe18--C4	{(-0.021, 0.008, 0.060)}	{( 0.019, 0.006, -0.038)}

The variation of the  $\Delta(BCP-RCP)$  with respect to the absence of the  $\mathbf{E}$ -field provides a way to determine the increase (positive values) or decrease (negative values) in the relative topological stability of  $BCP$ s when the  $\mathbf{E}$ -field is applied, see **Table 1**. The original  $BCP-RCP$  separations are provided in the **Supplementary Materials S8**. We see that the closed-shell H14--N16  $BCP$ , present for the forward minimum, is increasingly destabilized with the increase in the external (+) $\mathbf{E}$ -field from  $+20 \times 10^{-4}$  au to  $+40 \times 10^{-4}$  au. The corresponding application of increasing (-) $\mathbf{E}$ -field from  $-20 \times 10^{-4}$  au to  $-40 \times 10^{-4}$  au causes the relative stabilization to increase. The opposite effect occurs for the closed-shell H14--N13  $BCP$ , present for the reverse minimum: that is the increase/decrease in the magnitude of the external (+) $\mathbf{E}$ -field induces an increase/decrease in the relative stability of the H14--N13  $BCP$ . The shared-shell N16-H14  $BCP$  and shared-shell N13-H14  $BCP$  both display an order of magnitude smaller relative destabilization and stabilization effects due to being inherently stronger bonding interactions than the closed-shell H14--N16  $BCP$  and closed-shell H14--N13  $BCP$ . The increase in the relative stability of the Fe18--C1  $BCP$  for increase in the positive  $\mathbf{E}$ -field values is considerable, the converse being true for the Fe18--C4  $BCP$ . Weaker (opposite) effects are observed for the reverse IRC corresponding to the Fe18--C1  $BCP$  and Fe18--C4  $BCP$ . Therefore, the ‘OFF’ and ‘ON’ switch performance is in agreement with the results from the total local energy density  $H(\mathbf{r}_b)$  and  $\lambda_{3\sigma}$ .

#### 4.2 The switch performance and mechanism explained by the stress tensor trajectories $\mathbb{T}_\sigma(s)$

In this section we investigate the effect of the variation of the external  $\mathbf{E}$ -field on the ‘ON’ and ‘OFF’ functioning of the switch by examination of the stress tensor trajectories  $\mathbb{T}_\sigma(s)$  and the associated real space lengths ( $l$ ), see **Figure 3** and **Table 2** respectively and also refer to **Scheme 1** and the **Supplementary Materials S2**.

**Table 2.** The real space trajectory  $\mathbb{T}_\sigma(s)$  lengths  $l$  in au for the (r,f) i.e. the reverse (r = 'ON') and forward (f = 'OFF') directions respectively corresponding to values of the external  $\mathbf{E}$ -field = 0,  $\pm 20 \times 10^{-4}$  au and  $\pm 40 \times 10^{-4}$  au, see the caption of **Table 1** for further details. We also provide the real space  $l$  corresponding to the shift in the geometric centre (GC) of the H14 *NCP*.

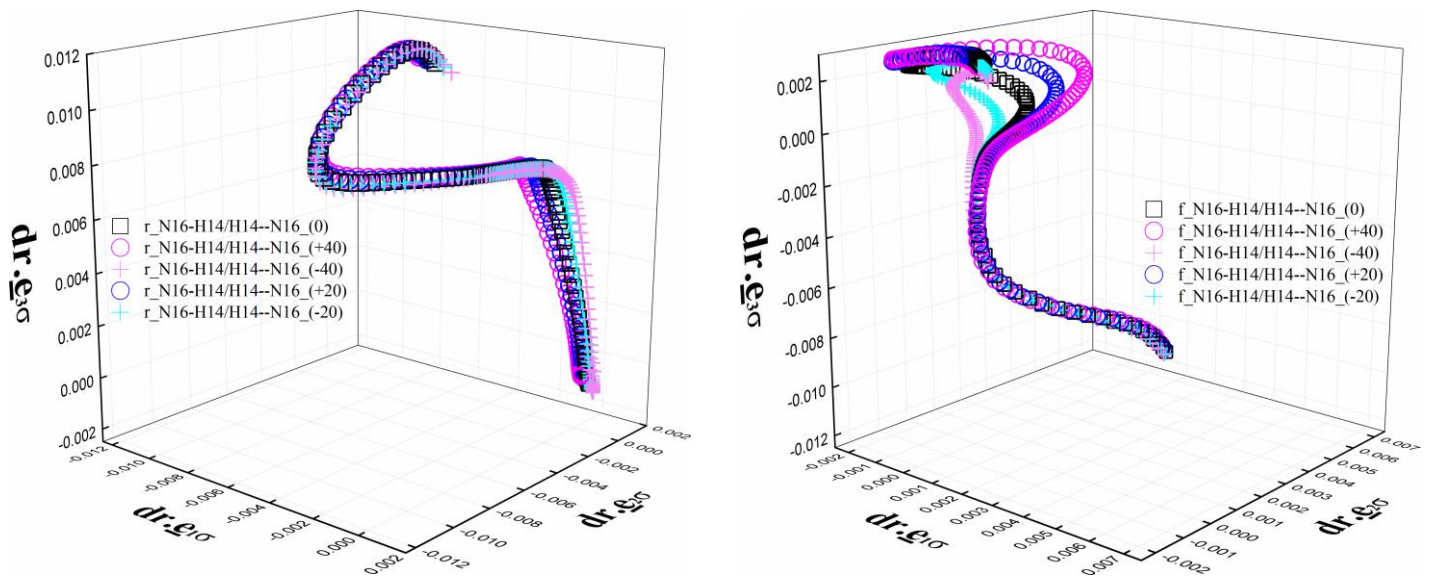
<i>BCP</i>	$l$				
	-40	+40	0	-20	+20
N13-H15	(0.668, 0.640)	(0.560, 0.684)	(0.610, 0.704)	(0.637, 0.681)	(0.584, 0.704)
<b>H14--N13/N13-H14</b>	(0.784, 0.783)	(0.591, 0.955)	(0.654, 0.891)	(0.701, 0.836)	(0.617, 0.930)
<b>N16-H14/H14--N16</b>	(1.129, 0.485)	(1.006, 0.577)	(1.054, 0.533)	(1.087, 0.510)	(1.025, 0.554)
N16-H17	(0.724, 0.775)	(0.631, 0.873)	(0.661, 0.811)	(0.689, 0.791)	(0.639, 0.838)
Fe18--C1	(0.197, 0.329)	(0.208, 0.292)	(0.197, 0.301)	(0.195, 0.311)	(0.202, 0.295)
Fe18--C4	(0.243, 0.266)	(0.251, 0.270)	(0.243, 0.271)	(0.242, 0.270)	(0.246, 0.271)
<b>H14 (GC)</b>	(1.484, 1.028)	(1.296, 1.252)	(1.375, 1.178)	(1.425, 1.109)	(1.330, 1.225)

Examination of the real space  $\mathbb{T}_\sigma(s)$  lengths  $l$  for the forward (f = 'OFF') direction of the H14--N16 *BCP* demonstrates that  $l$  increases with increase in (+) $\mathbf{E}$ -field values, and decreases with increases in the (-) $\mathbf{E}$ -field values, see **Table 2**. The converse is true for the  $l$  value of the shared-shell N16-H14 *BCP* associated with the reverse (r = 'ON') direction, where  $l$  decreases with increase in (+) $\mathbf{E}$ -field values, and increases with increases in the (-) $\mathbf{E}$ -field values. The same trends in the 'OFF' and 'ON' dependency on the  $\mathbf{E}$ -field are observed for the H14--N13/N13-H14 *BCP*.

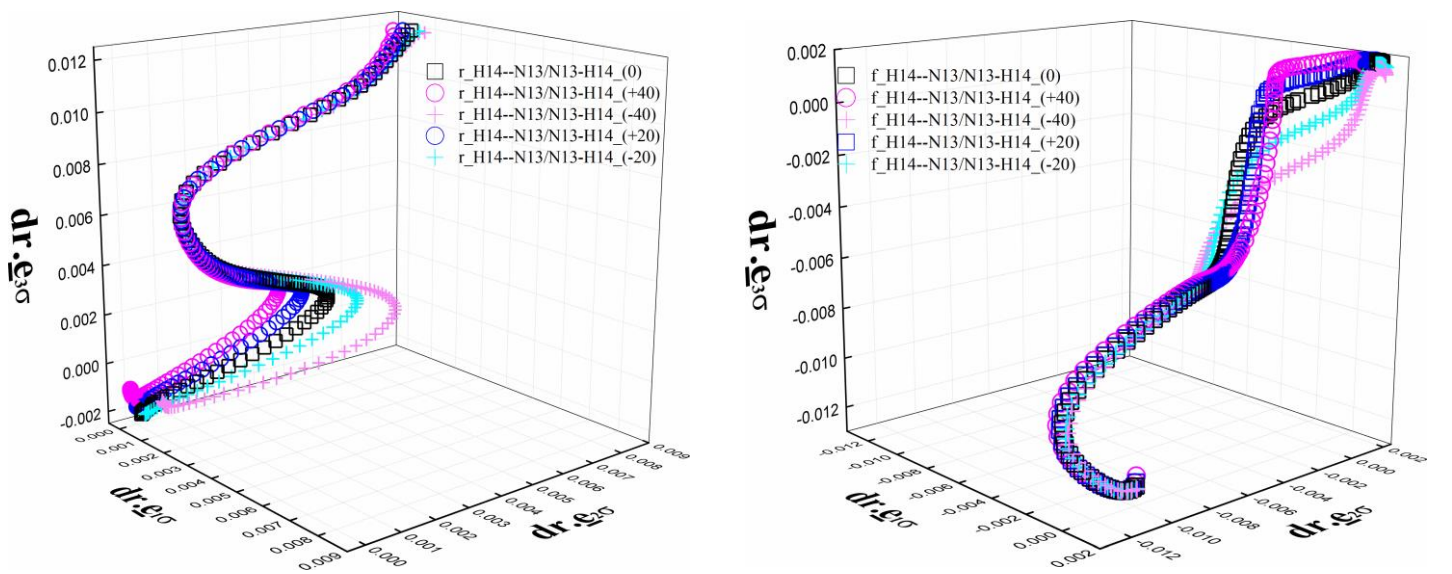
The changes in  $l$  are larger for the reverse 'ON' direction. The  $l$  associated with the  $\mathbb{T}_\sigma(s)$  of the facile H14 *NCP* are in agreement with the N16-H14/H14--N16 *BCP* and H14--N13/N13-H14 *BCP* with respect to the dependency of  $l$  on the  $\mathbf{E}$ -field and display a stronger effect for both the forward (f = 'OFF') and reverse (r = 'ON') directions.

The shared-shell N16-H17 *BCP* also displays an increase in  $l$  for the forward 'OFF' switch position with increase in the (+) $\mathbf{E}$ -field and decrease in  $l$  for increasing (-) $\mathbf{E}$ -field with the converse behavior corresponding to the 'ON' position. The facile H14 *NCP* is bonded to N16 which may explain why the dependency of  $l$  on the  $\mathbf{E}$ -field is present. This may explain why this dependency is not apparent for the N13-H15 *BCP*. The Fe18--C1 *BCP* and Fe18--C4 *BCP* also do not show this dependency on the  $\mathbf{E}$ -field, since they are too distant from the facile H14 *NCP*.

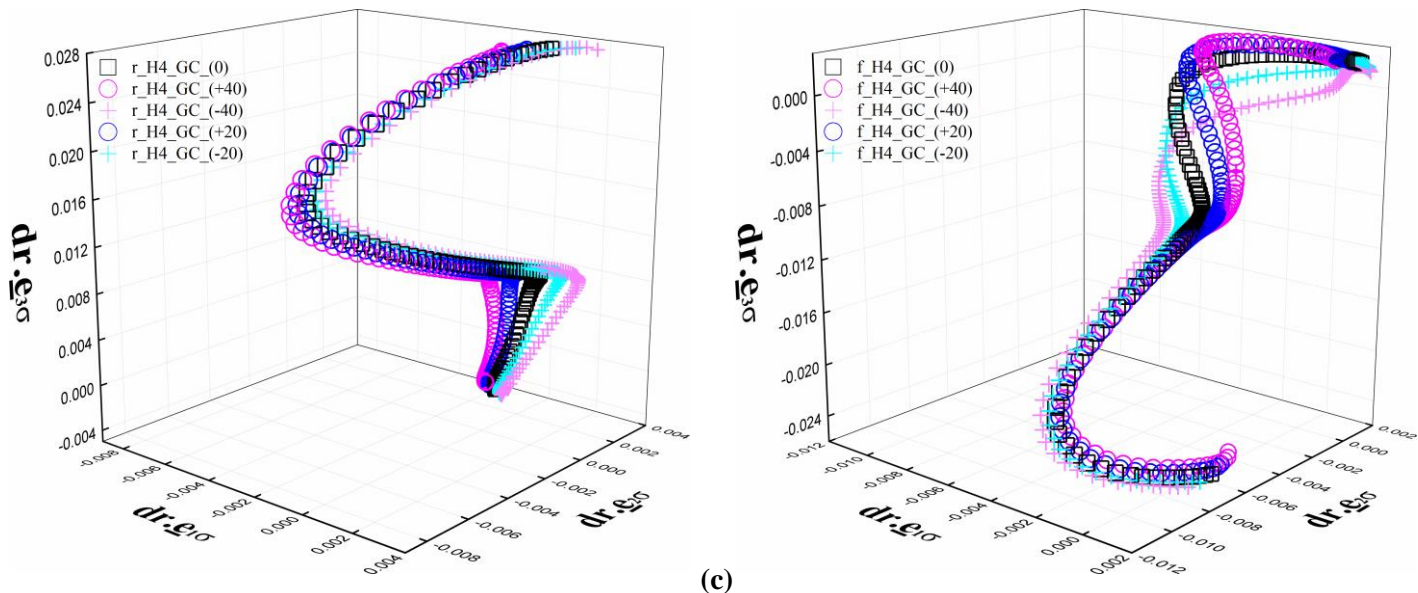
Examination of the  $\mathbb{T}_\sigma(s)$  associated with the N16-H14/H14--N16 *BCP* and H14--N13/N13-H14 *BCP* demonstrates a dependency on the magnitude and direction of the external  $\mathbf{E}$ -field, see **Figure 3**. The  $\mathbb{T}_\sigma(s)$ , particularly for the forward (f) ‘OFF’ switch position, displays the differences in  $l$  presented in **Table 2**. The  $\mathbb{T}_\sigma(s)$  of the H14 *NCP* emphasizes these differences; notice that the differences in the vertical axes are much larger than for the  $\mathbb{T}_\sigma(s)$  of the N16-H14/H14--N16 *BCP* and H14--N13/N13-H14 *BCP*, see **Figure 3(c)**. The reverse  $\mathbb{T}_\sigma(s)$  of the N16-H14 *BCP* most closely resembles the form of the reverse  $\mathbb{T}_\sigma(s)$  of the H14 *NCP*, compare the left panels of **Figure 3(a)** and **Figure 3(c)**. Similarly the forward  $\mathbb{T}_\sigma(s)$  of the H14--N16 *BCP* most closely resembles the forward  $\mathbb{T}_\sigma(s)$  of the H14 *NCP*, compare the right panels of **Figure 3(b)** and **Figure 3(c)**.



(a)

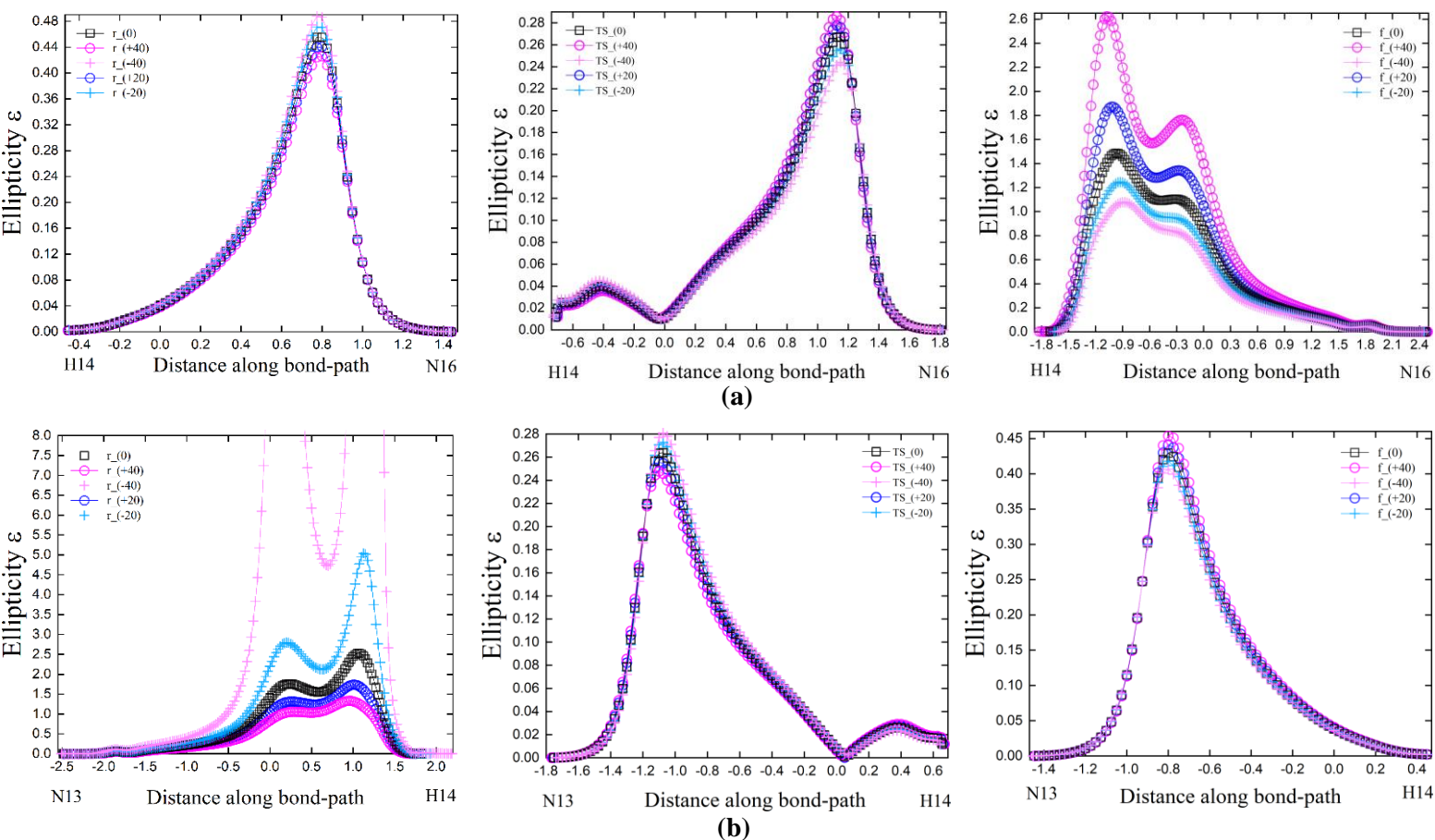


(b)



**Figure 3.** The stress tensor trajectories  $\mathbb{T}_\sigma(s)$  are presented for the reverse (r = 'ON' switch position) and forward (f = 'OFF' switch position) directions of the N16-H14/H14--N16 BCPs for values of the external electric  $\mathbf{E}$ -field;  $\mathbf{E} = 0, \pm 20 \times 10^{-4}$  au and  $\pm 40 \times 10^{-4}$  au, in the left and right panels respectively in sub-figure (a). The corresponding  $\mathbb{T}_\sigma(s)$  of the N13-H14/H14--N13 BCPs are presented in sub-figure (b). The corresponding  $\mathbb{T}_\sigma(s)$  for the geometric centre (GC) of the H14 atom for the r and f directions are presented in the left and right panels respectively of sub-figure (c). See **Scheme 1** for the BCP locations and the atom labels.

#### 4.3 Determination of the switch performance from the bond-path properties



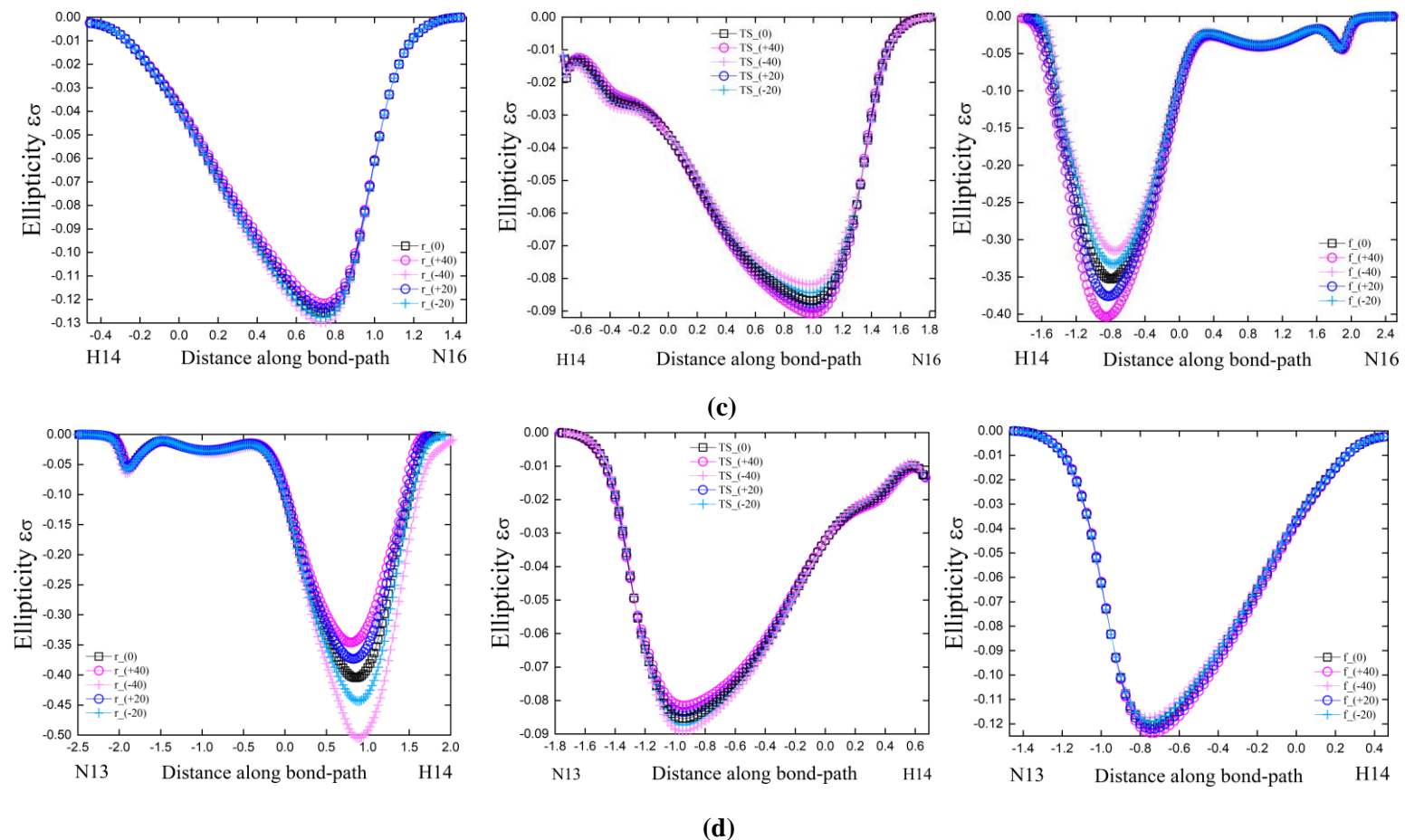


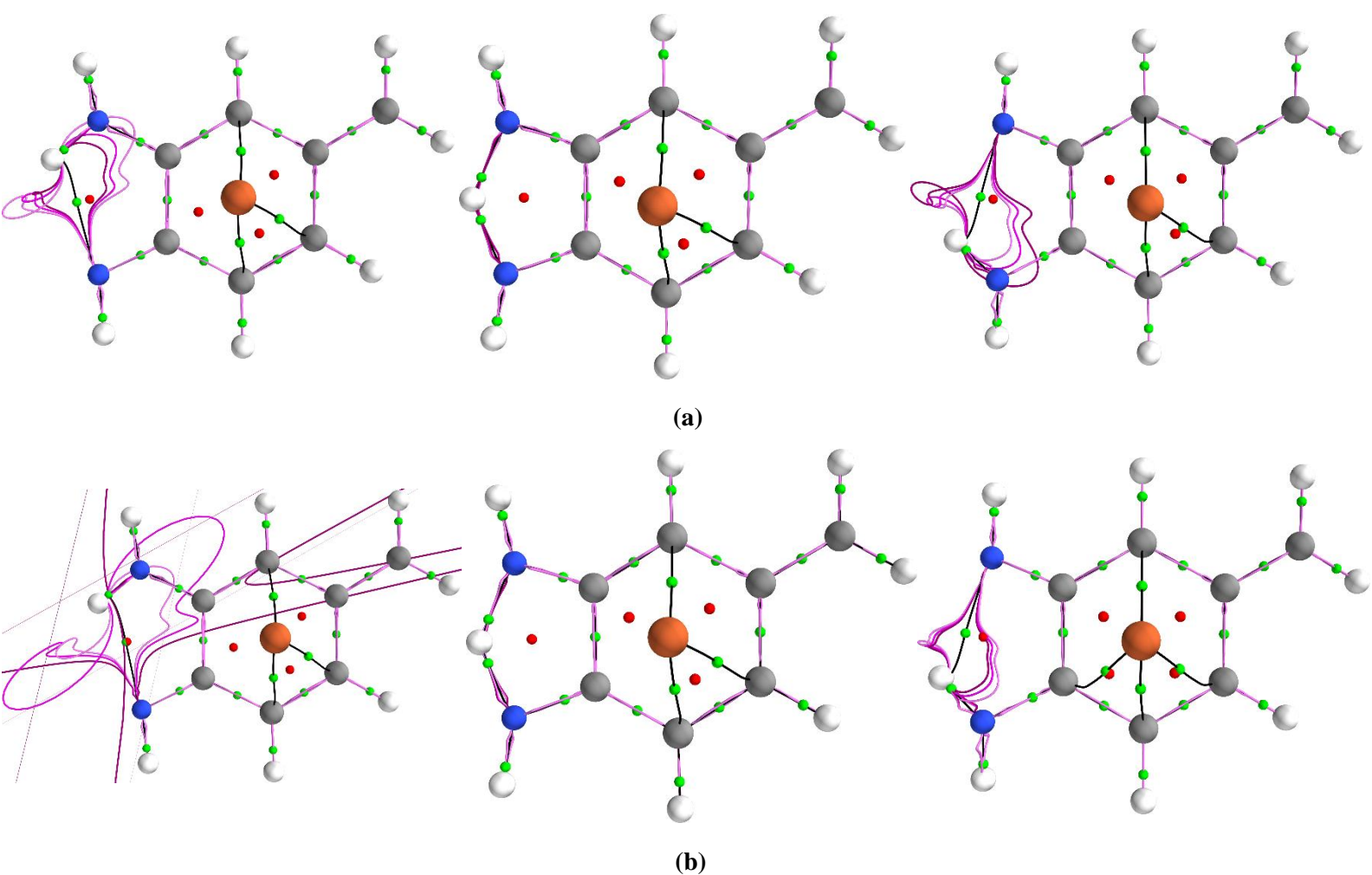
**Figure 4.** The variations of the ellipticity  $\varepsilon$  profiles with distance ( $\text{\AA}$ ) along the bond-path for the reverse (r), transition state (TS) and forward (f) directions for the values of the external  $\mathbf{E}$ -field;  $\mathbf{E} = 0, 20 \times 10^{-4}$  au and  $40 \times 10^{-4}$  au, associated with the N16-H14/H14--N16 BCPs are presented in the left, middle and right panels of sub-figure (a) respectively. The corresponding plots for the N13-H14/H14--N13 BCPs are presented in sub-figure (b). The corresponding plots for the stress tensor ellipticity  $\varepsilon_{\sigma}$  profiles are presented in the sub-figures (c) and (d) respectively. See **Scheme 1** for the BCP locations and the atom labels.

The ellipticity  $\varepsilon$  profile demonstrates the effect of the variation of the direction and magnitude of the external  $\mathbf{E}$ -field for the reverse minimum, transition state and forward minimum, on the N16-H14/H14--N16 BCP and H14--N13/N13-H14 BCP, see **Figure 4(a)**, **Figure 4(b)** respectively and the **Supplementary Materials S9**.

The ellipticity  $\varepsilon$  profile indicates a slight preference for stronger (-) $\mathbf{E}$ -fields for the reverse minimum of the shared-shell N16-H14 BCP, see the left panel of **Figure 4(a)**. For both the transition state and forward minimum that correspond to the closed-shell H14--N16 BCP there is a strong preference for stronger (+) $\mathbf{E}$ -fields, see the middle and right panels of **Figure 4(a)** respectively. The converse is true for the H14--N13/N13-H14 BCP transition from the reverse minimum through the transition state to the forward minimum, see **Figure 4(b)**. These results demonstrate that the transfer of the H14 NCP comprising the closed-shell H14--N16 BCP and the closed-shell H14--N13 BCP is facilitated the most by stronger (+) $\mathbf{E}$ -fields and (-) $\mathbf{E}$ -fields, respectively. The effect is larger for the H14 NCP when comprising the H14--N13 BCP than the H14--N16 BCP, i.e. the ‘ON’ and ‘OFF’ positions respectively. The corresponding results for the stress tensor ellipticity  $\varepsilon_{\sigma}$  are in qualitative agreement and are presented in **Figure 4(c)** and **Figure 4(d)**.

The forms of the  $\{q, q'\}$  path-packets, which define the most preferred directions of the  $\rho(\mathbf{r})$  motion, are shaped by the response of  $\rho(\mathbf{r})$ , which moves in the opposite direction to the applied  $\mathbf{E}$ -field as defined in **Scheme 1**, i.e. (+) $\mathbf{E}$ -field and (-) $\mathbf{E}$ -field are defined as parallel and anti-parallel to the direction of the C1-C2 *BCP* bond-path respectively, see **Figure 5**.

Larger  $\{q, q'\}$  path-packets that occur in the vicinity of the H14--N16 *BCP* in the case of an increase in the magnitude of the (+) $\mathbf{E}$ -field for the forward direction indicate a greater ease of movement and therefore improved performance of the switch in the 'OFF' position, see the right panel of **Figure 5(a)**. The converse is true for the N16-H14 *BCP*, where an increase in the magnitude of the (+) $\mathbf{E}$ -field indicates a deterioration in switch performance in the 'ON' position, see the left panel of **Figure 5(a)**. Larger  $\{q, q'\}$  path-packets that occur for an increase in the magnitude of the (-) $\mathbf{E}$ -field in the vicinity of the H14--N13 *BCP* for the reverse direction indicate a greater ease of movement and therefore improved performance of the switch in the 'ON' position, see the right panel of **Figure 5(b)**. The converse is true for the N13-H14 *BCP* for the forward direction, where an increase in the magnitude of the (-) $\mathbf{E}$ -field indicates a deterioration in switch performance in the 'OFF' position, see the left panel of **Figure 5(b)**. The stress tensor  $\{q_{\sigma}, q_{\sigma}'\}$  path-packets are consistent with the  $\{q, q'\}$  path-packets, see **Figure 5(c)** and **Figure 5(d)**.



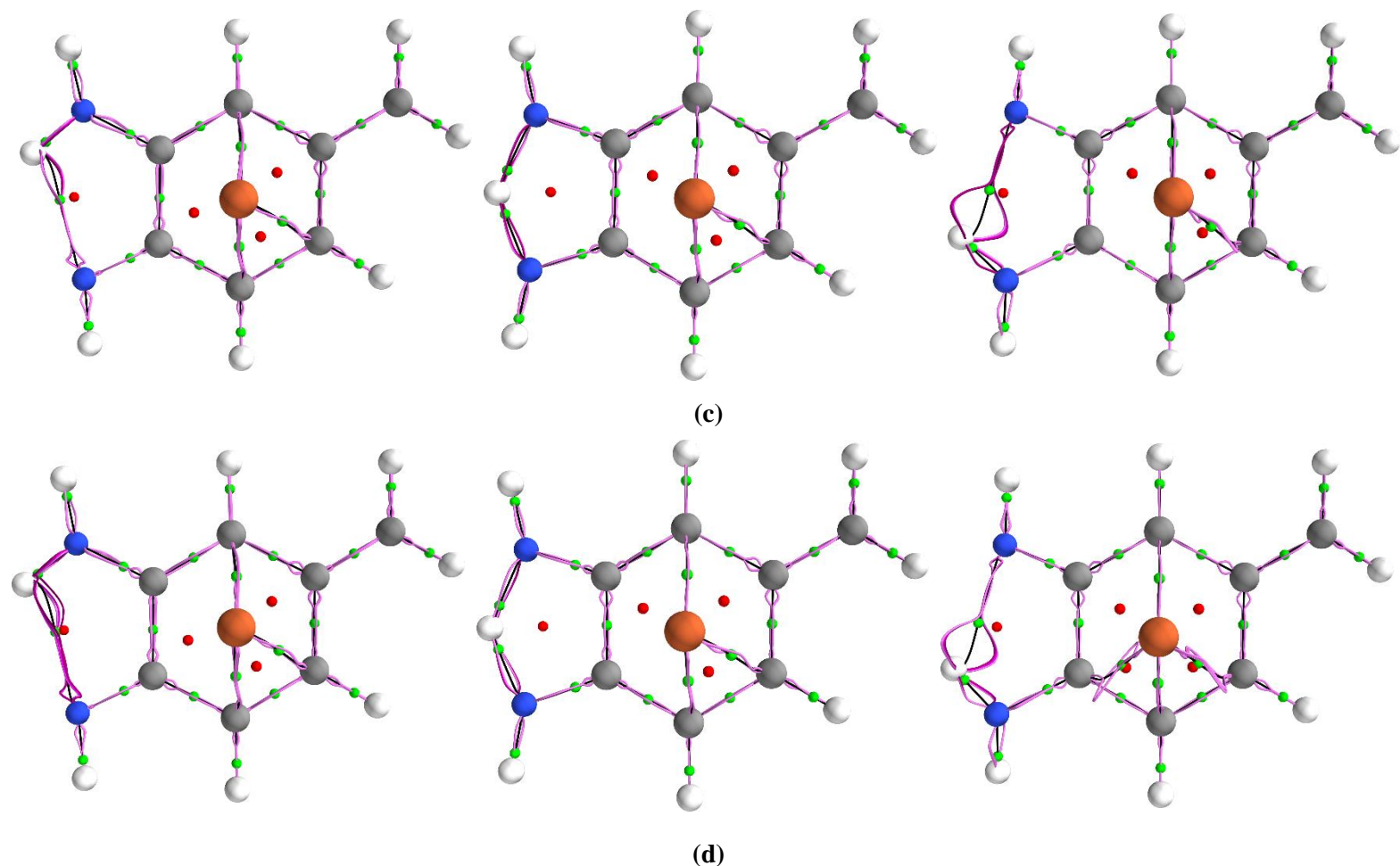


**Figure 5.** The bond-path framework sets  $\mathbb{B} = \{q, q', r\}$  i.e. the most preferred path-packets for the reverse (r), transition state (TS) and forward (f) directions are presented in the left, middle and right panels of sub-figure (a) respectively. Values of the external (+)E-field = 0,  $20 \times 10^{-4}$  au and  $40 \times 10^{-4}$  au, are indicated by dark-magenta, pale-magenta, and mid-magenta, respectively. The corresponding  $\{q, q'\}$  path-packets for the (-)E-field are presented in sub-figure (b). The corresponding results for the stress tensor  $\mathbb{B}_\sigma = \{q_\sigma, q'_\sigma, r\}$  are presented in sub-figures (c) and (d) respectively.

The external  $\mathbf{E}$ -field distorts the  $\mathbb{B} = \{q, q', r\}$  path-packets comprising the switch e.g. to stretch or compress the inter-nuclear separations (GBL), or the three paths  $p$ ,  $q$  and  $r$  corresponding to  $\mathbb{H}^*$ ,  $\mathbb{H}$  and the BPL respectively. The distortion produced depends on the relative parallel (+) or anti-parallel (-) orientation of the  $\mathbf{E}$ -field, see the theory section 2.2 and **Scheme 1** and the caption. We present the results relative to those of the switch in the absence of an external  $\mathbf{E}$ -field, see **Table 3**. The full version is provided in the **Supplementary Materials S10**.

The  $\mathbb{B} = \{q, q', r\}$  and  $\mathbb{B}_\sigma = \{q_\sigma, q'_\sigma, r\}$  path-packets, of the most preferred directions of motion, orientated parallel (+)/anti-parallel (-) to the direction of  $\mathbf{E}$ -field are stretched/compressed relative to the absence of the external  $\mathbf{E}$ -field. The distortions induced for a given value of the external  $\mathbf{E}$ -field, are larger for the BPL than the GBL.

**Table 3.** The variation of the differences in lengths of eigenvector following path lengths  $\Delta\{\mathbb{H},\mathbb{H}^*\}$ , the bond-path lengths  $\Delta\{\text{BPL}\}$  corresponding to the  $\mathbf{q}$  and  $\mathbf{p}$ ' paths and  $\Delta\{\mathbb{H}_\sigma,\mathbb{H}_\sigma^*\}$  for the stress tensor  $\mathbf{q}_\sigma$  and  $\mathbf{p}'_\sigma$  paths, respectively see **Scheme 1**, with values of the external  $\mathbf{E}$ -field =  $\pm 20 \times 10^{-4}$  au and  $\pm 40 \times 10^{-4}$  au. In addition, the inter-nuclear  $NCP$ - $NCP$  separations  $\Delta\{\text{GBL}\}$  are provided. All units are in au. The  $\mathbf{E}$ -field = 0 values are subtracted for each of the (r,TS,f) sets corresponding to the reverse (r) minimum, transition state (TS) and forward (f) minimum.

<i>BCP</i>	$\Delta\{\mathbb{H}\}$		$\Delta\{\mathbb{H}^*\}$		$\Delta\{\mathbb{H}\}$		$\Delta\{\mathbb{H}^*\}$		
					-20				
N13-H15	{( 0.007, 0.007,-0.011)}		{( 0.007, 0.007,-0.011)}		{(-0.006,-0.007, 0.004)}		{(-0.006,-0.007, 0.005)}		
H14--N13/N13-H14	{( 6.168,-0.007,-0.007)}		{( 5.699,-0.007,-0.006)}		{(-1.891, 0.007, 0.006)}		{(-1.669, 0.008, 0.007)}		
N16-H14/H14--N16	{( 0.006,-0.004,-0.655)}		{(-0.045, 0.058,-0.553)}		{(-0.006,-0.007, 1.426)}		{(-0.005,-0.007, 1.231)}		
N16-H17	{( 0.013,-0.011,-0.009)}		{( 0.013,-0.011,-0.009)}		{(-0.008, 0.012, 0.011)}		{(-0.009, 0.012, 0.011)}		
-40									
N13-H15	{( 0.015, 0.015,-0.029)}		{( 0.014, 0.014,-0.029)}		{(-0.011,-0.014, 0.004)}		{(-0.011,-0.013, 0.005)}		
H14--N13/N13-H14	{(11396,-0.012,-0.011)}		{(11395,-0.013,-0.281)}		{(-2.753, 0.008, 0.009)}		{(-2.393, 0.016, 0.016)}		
N16-H14/H14--N16	{( 0.012, 0.002,-1.027)}		{(-0.039, 0.062,-0.846)}		{(-0.011,-0.013, 4.301)}		{(-0.011,-0.014, 3.814)}		
N16-H17	{( 0.028,-0.021,-0.017)}		{( 0.027,-0.021,-0.017)}		{(-0.013, 0.023, 0.021)}		{(-0.014, 0.023, 0.022)}		
$\Delta\{\text{BPL}\}$									
-20									
+20									
N13-H15	{( 0.001, 0.000, 0.001)}		{( 0.000, 0.001,-0.001)}		{( 0.000,-0.001, 0.001)}		{( 0.000, 0.001, -0.001)}		
H14--N13/N13-H14	{( 0.111,-0.014, 0.004)}		{(-0.083, 0.015,-0.004)}		{( 0.035,-0.013, 0.003)}		{(-0.035, 0.014,-0.003)}		
N16-H14/H14--N16	{(-0.003, 0.016,-0.057)}		{( 0.003,-0.016, 0.066)}		{(-0.003, 0.015,-0.034)}		{( 0.003,-0.014, 0.035)}		
N16-H17	{(-0.001, 0.000,-0.001)}		{( 0.002, 0.000, 0.001)}		{(-0.001, 0.000,-0.001)}		{( 0.001, 0.000, 0.001)}		
$\Delta\{\text{GBL}\}$									
-20									
+20									
N13-H15	{( 0.002,-0.001, 0.003)}		{(-0.001, 0.001,-0.002)}		{( 0.001,-0.001, 0.002)}		{(-0.001, 0.002,-0.002)}		
H14--N13/N13-H14	{( 0.378,-0.026, 0.007)}		{(-0.152, 0.029,-0.006)}		{( 0.069,-0.025, 0.007)}		{(-0.069, 0.027,-0.006)}		
N16-H14/H14--N16	{(-0.006, 0.032,-0.106)}		{( 0.006,-0.028, 0.144)}		{(-0.006, 0.031,-0.066)}		{( 0.006,-0.027, 0.072)}		
N16-H17	{(-0.003, 0.000,-0.001)}		{( 0.004, 0.000, 0.002)}		{(-0.002, 0.001,-0.001)}		{( 0.003, 0.000, 0.002)}		
$\Delta\{\text{BPL}\}$									
-40									
+40									
N13-H15	{( 0.002,-0.001, 0.003)}		{(-0.001, 0.001,-0.002)}		{( 0.001,-0.001, 0.002)}		{(-0.001, 0.002,-0.002)}		
H14--N13/N13-H14	{( 0.378,-0.026, 0.007)}		{(-0.152, 0.029,-0.006)}		{( 0.069,-0.025, 0.007)}		{(-0.069, 0.027,-0.006)}		
N16-H14/H14--N16	{(-0.006, 0.032,-0.106)}		{( 0.006,-0.028, 0.144)}		{(-0.006, 0.031,-0.066)}		{( 0.006,-0.027, 0.072)}		
N16-H17	{(-0.003, 0.000,-0.001)}		{( 0.004, 0.000, 0.002)}		{(-0.002, 0.001,-0.001)}		{( 0.003, 0.000, 0.002)}		
$\Delta\{\mathbb{H}_\sigma\}$									
-20									
+20									
N13-H15	{( 0.000,-0.001,-0.001)}		{( 0.000, 0.000, 0.000)}		{( 0.000, 0.000, 0.000)}		{( 0.000, 0.000, 0.000)}		
H14--N13/N13-H14	{(-0.017,-0.014, 0.003)}		{(-0.016,-0.014, 0.004)}		{( 0.015, 0.015,-0.003)}		{( 0.014, 0.014,-0.003)}		
N16-H14/H14--N16	{(-0.002, 0.014, 0.013)}		{(-0.003, 0.015, 0.014)}		{( 0.002,-0.015,-0.015)}		{( 0.002,-0.015,-0.017)}		
N16-H17	{(-0.001, 0.000, 0.000)}		{(-0.001, 0.000, 0.000)}		{( 0.000, 0.001, 0.001)}		{( 0.000, 0.001, 0.001)}		
$\Delta\{\mathbb{H}_\sigma^*\}$									
-40									
+40									
N13-H15	{( 0.000, 0.000, 0.000)}		{( 0.000, 0.000, 0.000)}		{( 0.001, 0.000, 0.000)}		{( 0.001, 0.000, 0.001)}		
H14--N13/N13-H14	{(-0.032,-0.027, 0.006)}		{(-0.031,-0.026, 0.007)}		{( 0.029, 0.029,-0.006)}		{( 0.027, 0.028,-0.005)}		
N16-H14/H14--N16	{(-0.004, 0.029, 0.024)}		{(-0.005, 0.031, 0.026)}		{( 0.005,-0.031,-0.032)}		{( 0.005,-0.029,-0.034)}		
N16-H17	{(-0.001, 0.000, 0.000)}		{(-0.001,-0.001, 0.000)}		{( 0.001, 0.002, 0.002)}		{( 0.001, 0.002, 0.002)}		

## 5. Conclusions

The ability to visualize and quantify changes to the switch topology using the next generation QTAIM analysis provides new insights into the reasons for the improved ‘ON’ and ‘OFF’ functioning of the switch from the position corresponding to the tautomerization barrier.

The total local energy  $H(\mathbf{r}_b)$  and stress tensors eigenvalue  $\lambda_{3\sigma}$  results demonstrate that the H14--N16 *BCP* weakens and is destabilized by an increase in the (+) $\mathbf{E}$ -field, thus rendering the switch easier to move from the energetic transition state to the ‘OFF’ position and ultimately increase a better performing switch. The converse is true for an increase in the (-) $\mathbf{E}$ -field, i.e. the H14--N16 *BCP* strengthens and is stabilized. In addition, the H14--N13 *BCP* is weakened and destabilized resulting in a switch with improved performance in the ‘ON’ position. This assessment of the switch performance in the ‘ON’ position was not accessible from inspection of the variation of the relative energy  $\Delta E$  plots because there is no variation with respect to the applied  $\mathbf{E}$ -field. The relative energy plots also cannot shed light on the *mechanism* of the switching process because they are unable to quantify changes in the chemical behavior incurred by the motion of the H14 atom along the hydrogen bond participating in the tautomerization process.

Greater stabilities from the relative energy  $\Delta E$  values were found to correlate with a greater persistence of the metallic H16--N14 *BCP* along the forward direction of the IRC. This suggests that the H14 *NCP* transfer tautomerization is facilitated by the presence of a more metallic H16--N14 *BCP* where the metallicity  $\xi(\mathbf{r}_b)$  was maximized in presence of larger (+) $\mathbf{E}$ -fields. Conversely, the H14 *NCP* transfer tautomerization was found to be hindered by the presence of larger (-) $\mathbf{E}$ -fields. Therefore, the metallicity  $\xi(\mathbf{r}_b)$  values explain why the presence of larger (+) $\mathbf{E}$ -fields facilitates the H14 *NCP* transfer tautomerization by the greater destabilization of the H16--N14 *BCP* bond-path, enabling easier motion of the H14 *NCP*. Therefore, larger (-) $\mathbf{E}$ -fields hinder the H14 *NCP* transfer tautomerization by reduced destabilization of the H16--N14 *BCP* bond-path. The variation of  $\Delta(\text{BCP-RCP})$  with respect to the absence of the  $\mathbf{E}$ -field also provides a way to determine the increase (positive values) or decrease (negative values) in the relative topological stability of *BCPs* when the  $\mathbf{E}$ -field is applied.

The real space  $\mathbb{T}_\sigma(s)$  lengths  $l$  demonstrate the dependency of  $l$  of the ‘ON’ and ‘OFF’ switch positions on the (+) $\mathbf{E}$ -field values; the functioning of the ‘ON’ and ‘OFF’ switch positions are improved by increases in (-) $\mathbf{E}$ -field and (+) $\mathbf{E}$ -field respectively. The ability to visualize and quantify the QTAIM bond-path framework set  $\mathbb{B}$  and stress tensor  $\mathbb{B}_\sigma$  provides new insights into the reasons for the improved ‘ON’ and ‘OFF’ functioning of the switch from the position corresponding to the tautomerization barrier. The forms of the  $\{\mathbf{q}, \mathbf{q}'\}$  path-packets were shaped by the response of  $\rho(\mathbf{r})$  to a change in direction of the applied  $\mathbf{E}$ -field. This provides a novel method to visualize the effects of the applied  $\mathbf{E}$ -field. The effects were quantified in terms of the differences in the eigenvector following path lengths  $\Delta\{\mathbb{H}, \mathbb{H}^*\}$ , the bond-path lengths  $\Delta\{\text{BPL}\}$  that correspond to the  $\mathbf{q}$  and  $\mathbf{p}'$  paths and  $\Delta\{\mathbb{H}_\sigma, \mathbb{H}_\sigma^*\}$  for the stress tensor  $\mathbf{q}_\sigma$  and  $\mathbf{p}'_\sigma$  paths, respectively. The

larger distortions induced for a given value of the external  $\mathbf{E}$ -field for the BPL compared with the GBL demonstrates that the BPL provides more information about the distortion along the bond length.

Improved 'OFF' switch function was provided by larger (+) $\mathbf{E}$ -field values that enable the H14 *NCP* tautomerization to occur more readily by destabilizing the closed-shell H14--N16 *BCP* bond-path that exists from the transition state to the forward minimum, relative to the absence of an  $\mathbf{E}$ -field. The functioning of the switch to the 'OFF' position is worsened by the application of larger (-) $\mathbf{E}$ -fields that stabilize the H14--N16 *BCP* bond-path relative to the absence of an  $\mathbf{E}$ -field. Improved 'ON' switch functioning is provided by the application of the (-) $\mathbf{E}$ -field to the closed-shell H14--N13 *BCP* that exists for the transition state and the reverse minimum. The functioning of the switch to the 'ON' position is worsened by the application of larger (+) $\mathbf{E}$ -fields that stabilize the H14--N13 *BCP* bond-path relative to the absence of an  $\mathbf{E}$ -field.

Consistency of the factors affecting the 'ON' and 'OFF' switch performance was found from all the *BCP* measures:  $H(\mathbf{r}_b)$ ,  $\lambda_{3\sigma}$ , metallicity  $\xi(\mathbf{r}_b)$ ,  $\Delta(\text{BCP-RCP})$ ,  $\mathbb{T}_\sigma(s)$  with associated lengths  $l$  and bond-path measures i.e. the relative lengths  $\Delta\{\mathbb{H}, \mathbb{H}^*\}$ , bond-path lengths  $\Delta\{\text{BPL}\}$ ,  $\Delta\{\mathbb{H}_\sigma, \mathbb{H}_\sigma^*\}$  and the  $\{q, q'\}$  and  $\{q_\sigma, q_\sigma'\}$  path-packets from QTAIM and the stress tensor.

The ultimate aim of this research is to design a molecular electronic circuit, which would consist of assemblies of connected molecular switches. This will require investigating the changes in switch behavior if multiple molecular switches are connected by molecular wires. As demonstrated in the current investigation, next-generation QTAIM analysis has the ability to provide insights into switch performance currently not attainable by other theoretical approaches. This will guide experimental investigations into building molecular electronic circuits.

## Acknowledgements

The National Natural Science Foundation of China is acknowledged, project approval number: 21673071. The One Hundred Talents Foundation of Hunan Province are gratefully acknowledged for the support of S.J. and S.R.K. The Royal Society is thanked by S.J., S.R.K, T.X, T.v.M and H.F. for support through an International Exchanges grant. We thank EaStCHEM for computational support via the EaStCHEM Research Computing Facility.

## References

- [1] A. Aviram, M. A. Ratner, *Chemical Physics Letters* **1974**, 29, 277–283.
- [2] M. A. Ratner, *Materials Today* **2002**, 5, 20–27.
- [3] G. E. Moore, *Proceedings of the IEEE* **1998**, 86, 82–85.
- [4] Y. Komoto, S. Fujii, M. Iwane, M. Kiguchi, *J. Mater. Chem. C* **2016**, 4, 8842–8858.
- [5] J. L. Zhang, J. Q. Zhong, J. D. Lin, W. P. Hu, K. Wu, G. Q. Xu, A. T. S. Wee, W. Chen, *Chem. Soc. Rev.* **2015**, 44, 2998–3022.
- [6] Z. Medin, D. Lai, *Phys. Rev. A* **2006**, 74, 062507.
- [7] W. Haiss, H. van Zalinge, S. J. Higgins, D. Bethell, H. Höbenreich, D. J. Schiffrin, R. J. Nichols, *J. Am. Chem. Soc.* **2003**, 125, 15294–15295.

- [8] H. Fruchtl, T. van Mourik, *arXiv:1801.01001 [physics]* **2018**.
- [9] C. Foroutan-Nejad, V. Andrushchenko, M. Straka, *Phys. Chem. Chem. Phys.* **2016**, *18*, 32673–32677.
- [10] T. Xu, L. Wang, Y. Ping, T. van Mourik, H. Fruchtl, S. R. Kirk, S. Jenkins, *International Journal of Quantum Chemistry* **2018**, *118*, e25676.
- [11] R. S. Judson, H. Rabitz, *Phys. Rev. Lett.* **1992**, *68*, 1500–1503.
- [12] M. Yu. Ivanov, D. R. Matusek, J. S. Wright, *Phys. Rev. A* **1996**, *54*, 5159–5170.
- [13] M. Dantus, V. V. Lozovoy, *Chem. Rev.* **2004**, *104*, 1813–1860.
- [14] A. D. Bandrauk, E.-W. S. Sedik, C. F. Matta, *Molecular Physics* **2006**, *104*, 95–102.
- [15] A. A. Arabi, C. F. Matta, *Phys. Chem. Chem. Phys.* **2011**, *13*, 13738–13748.
- [16] S. Sowlati-Hashjin, C. F. Matta, *J. Chem. Phys.* **2013**, *139*, 144101.
- [17] A. Saenz, *Phys. Rev. A* **2002**, *66*, 063407.
- [18] A. Saenz, *Phys. Rev. A* **2000**, *61*, 051402.
- [19] S. Petretti, Y. V. Vanne, A. Saenz, A. Castro, P. Decleva, *Phys. Rev. Lett.* **2010**, *104*, 223001.
- [20] M. Novák, C. Foroutan-Nejad, R. Marek, *J. Chem. Theory Comput.* **2016**, *12*, 3788–3795.
- [21] C. Foroutan-Nejad, R. Marek, *Phys. Chem. Chem. Phys.* **2014**, *16*, 2508–2514.
- [22] C. Foroutan-Nejad, M. Novák, R. Marek, *J. Phys. Chem. C* **2015**, *119*, 5752–5754.
- [23] Z. Wang, D. Danovich, R. Ramanan, S. Shaik, *J. Am. Chem. Soc.* **2018**, *140*, 13350–13359.
- [24] S. Shaik, R. Ramanan, D. Danovich, D. Mandal, *Chem. Soc. Rev.* **2018**, *47*, 5125–5145.
- [25] S. Shaik, D. Mandal, R. Ramanan, *Nature Chemistry* **2016**, *8*, 1091–1098.
- [26] W. J. Huang, T. Xu, S. R. Kirk, S. Jenkins, *Chemical Physics Letters* **2018**, *710*, 31–38.
- [27] P. Yang, T. Xu, R. Momen, A. Azizi, S. R. Kirk, S. Jenkins, *International Journal of Quantum Chemistry* **2018**, *118*, e25565.
- [28] M. X. Hu, T. Xu, R. Momen, G. Huan, S. R. Kirk, S. Jenkins, M. Filatov, *Journal of Computational Chemistry* **2016**, *37*, 2588–2596.
- [29] T. Xu, J. H. Li, R. Momen, W. J. Huang, S. R. Kirk, Y. Shigeta, S. Jenkins, *J. Am. Chem. Soc.* **2019**, DOI 10.1021/jacs.9b00823.
- [30] R. F. W. Bader, *Atoms in Molecules: A Quantum Theory*, Oxford University Press, USA, **1994**.
- [31] R. F. W. Bader, *J. Phys. Chem. A* **1998**, *102*, 7314–7323.
- [32] R. F. W. Bader, *J. Phys. Chem. A* **2009**, *113*, 10391–10396.
- [33] E. Kraka, D. Cremer, *Journal of Molecular Structure: THEOCHEM* **1992**, *255*, 189–206.
- [34] S. Jenkins, L. Blancafort, S. R. Kirk, M. J. Bearpark, *Phys. Chem. Chem. Phys.* **2014**, *16*, 7115–7126.
- [35] S. Jenkins, *J. Phys.: Condens. Matter* **2002**, *14*, 10251–10263.
- [36] S. Jenkins, P. W. Ayers, S. R. Kirk, P. Mori-Sánchez, A. Martín Pendás, *Chemical Physics Letters* **2009**, *471*, 174–177.
- [37] P. W. Ayers, S. Jenkins, *Computational and Theoretical Chemistry* **2015**, *1053*, 112–122.
- [38] A. Guevara-García, E. Echegaray, A. Toro-Labbe, S. Jenkins, S. R. Kirk, P. W. Ayers, *J. Chem. Phys.* **2011**, *134*, 234106.
- [39] P. W. Ayers, S. Jenkins, *J. Chem. Phys.* **2009**, *130*, 154104.
- [40] A. Guevara-García, P. W. Ayers, S. Jenkins, S. R. Kirk, E. Echegaray, A. Toro-Labbe, in *Electronic Effects in Organic Chemistry* (Ed.: B. Kirchner), Springer Berlin Heidelberg, Berlin, Heidelberg, **2014**, pp. 103–124.
- [41] R. F. W. Bader, T. T. Nguyen-Dang, in *Advances in Quantum Chemistry* (Ed.: P.-O. Löwdin), Academic Press, **1981**, pp. 63–124.
- [42] R. F. W. Bader, *J. Chem. Phys.* **1980**, *73*, 2871–2883.
- [43] L. Wang, G. Huan, R. Momen, A. Azizi, T. Xu, S. R. Kirk, M. Filatov, S. Jenkins, *J. Phys. Chem. A* **2017**, *121*, 4778–4792.
- [44] H. Guo, A. Morales - Bayuelo, T. Xu, R. Momen, L. Wang, P. Yang, S. R. Kirk, S. Jenkins, *Journal of Computational Chemistry* **2016**, *37*, 2722–2733.
- [45] S. Jenkins, M. I. Heggie, *Journal of Physics Condensed Matter* **2000**, *12*, 10325.
- [46] S. Jenkins, I. Morrison, *Chemical Physics Letters* **2000**, *317*, 97–102.
- [47] M. Frisch, G. Trucks, H. Schlegel, G. Scuseria, M. Robb, J. Cheeseman, G. Scalmani, V. Barone, B. Mennucci, G. Petersson, et al., *Gaussian 09, Revision B.01*, Gaussian, Inc., Wallingford, CT 06492 USA, **2009**.

- [48] C. Adamo, V. Barone, *J. Chem. Phys.* **1999**, *110*, 6158–6170.
- [49] T. H. Dunning, *J. Chem. Phys.* **1989**, *90*, 1007–1023.
- [50] S. Grimme, J. Antony, S. Ehrlich, H. Krieg, *J. Chem. Phys.* **2010**, *132*, 154104.
- [51] S. Grimme, S. Ehrlich, L. Goerigk, *Journal of Computational Chemistry* **2011**, *32*, 1456–1465.
- [52] T. A. Keith, *AIMAll*, Revision 17.01.25, TK Gristmill Software, Overland Park KS, USA, **2017**.